Supplementary Information for:

Enabling ionic transport in Li_3AlP_2: the roles of defects and disorder

Ji Hu,[1,2] Alexander G. Squires,[3] Jędrzej Kondek,[5,6,7] Michael J. Johnson,[1] Arthur B. Youd,[4] Pooja Vadhva,[1] Partha Paul,[8,9] Philip J. Withers,[9] Marco Di Michiel,[8] Dean Keeble,[10] Michael Ryan Hansen,[5,6] David O. Scanlon,[2,3,*] Alexander J. E. Rettie,[1,2,*]

[1] Electrochemical Innovation Laboratory, Department of Chemical Engineering, University College London, London, UK, WC1E 7JE
[2] The Faraday Institution, Quad One, Harwell Science and Innovation Campus, Didcot OX11 0RA, UK
[3] School of Chemistry, University of Birmingham, Edgbaston, Birmingham, B15 2TT, UK
[4] Department of Chemistry, University College London, London WC1H 0AJ, UK
[5] Institute of Physical Chemistry, University of Münster, Corrensstrasse 28/30, 48149 Münster, Germany
[6] Institute of Inorganic and Analytical Chemistry, University of Münster, Corrensstrasse 28, Münster, 48149, Germany
[7] International Graduate School for Battery Chemistry, Characterization, Analysis, Recycling and Application (BACCARA), University of Münster, Münster, 48149, Germany
[8] ESRF - The European Synchrotron, 71 Avenue des Martyrs, Grenoble, 3800, France
[9] Henry Royce Institute, Department of Materials, The University of Manchester, Manchester, M139PL, United Kingdom
[10] Diamond Light Source Ltd., Diamond House, Harwell Science and Innovation Campus, Didcot OX11 0DE, UK
* Corresponding authors (d.scanlon@ucl.ac.uk; a.rettie@ucl.ac.uk)

S1 Computational analysis

S1.1 Electronic and phonon band structure calculations

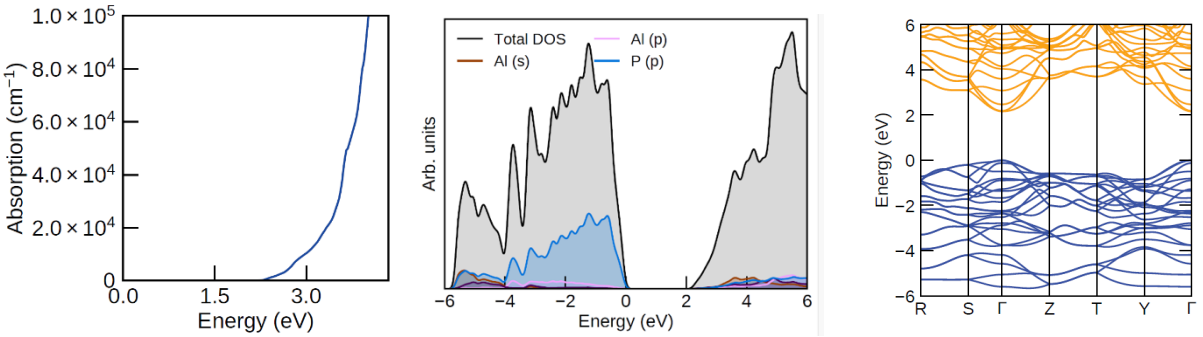

Figure S1.1. Optical absorption spectrum, electronic band structure and element-projected density of states of Li_3AlP_2. Indirect bandgap of 2.2 eV and direct bandgap of 2.36 eV.

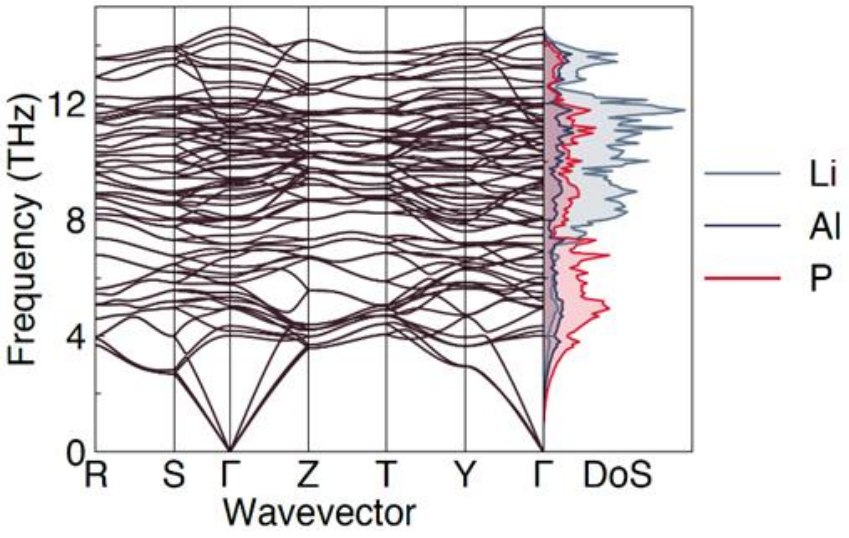

Figure S1.2. Phonon band structure of a 207 atom supercell of Li_3AlP_2 with the element-projected density of states.

S1.2 NEB calculations and interstitial defects

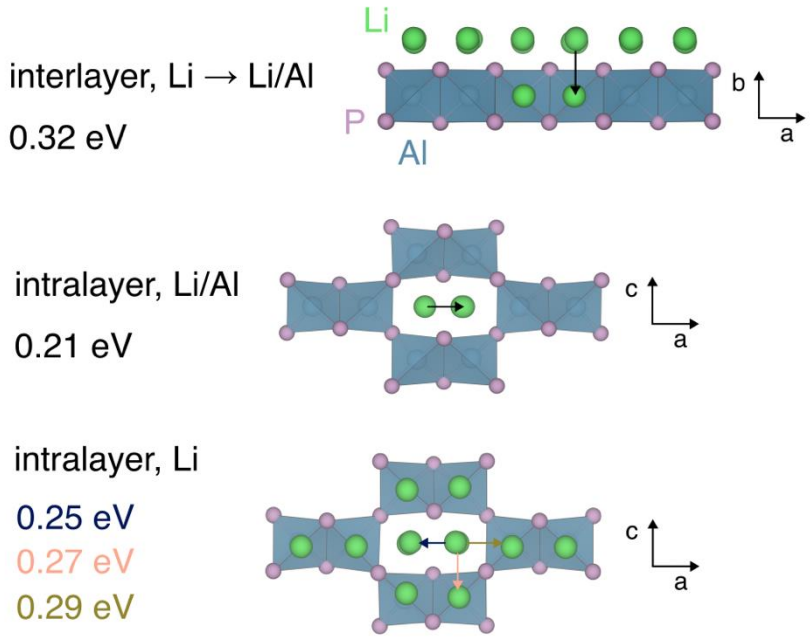

Figure S1.3. Schematics for vacancy-mediated ion migration pathways in Li_3AlP_2. The energy profiles for these pathways can be found in Figure 4 in the main manuscript.

The energy profiles for the vacancy-mediated hops are shown in Figure S1.3. To confirm vacancy transport as the majority diffusion mechanism in Li_3AlP_2, we carried out interstitial migration calculations, comparing a direct interstitial and intersticialcy diffusion, finding these barriers to be significantly higher than both the activation barriers calculated from the NMR experiments and the vacancy climbing image NEB calculations (Figure S1.4). The two interstitial sites are shown in Figure S1.5 and the mechanism is illustrated in Figure S1.6. The assumption is that any interstitial transport will be mediated by the lower energy defect site, site i.[1]

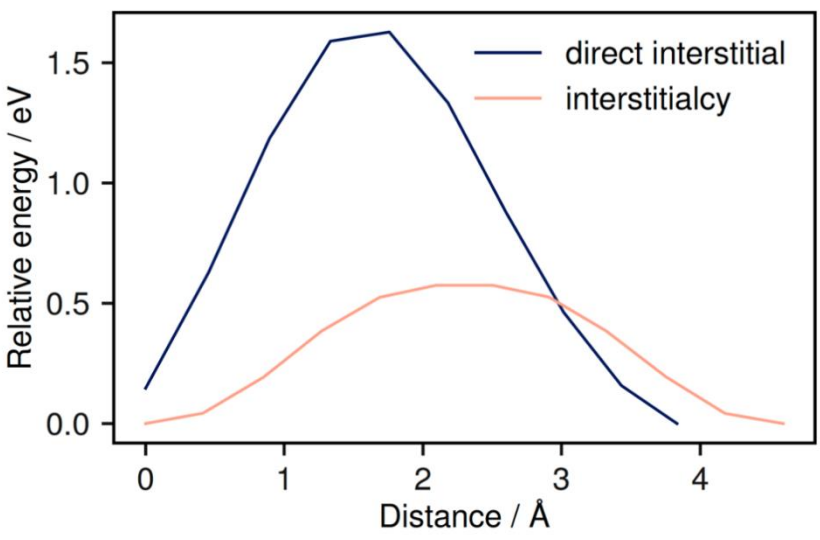

Figure S1.6. Activation energy of lithium hopping for interstitial defects in Li_3AlP_2. The migration path for the interstitials are represented schematically in figure S1.5.

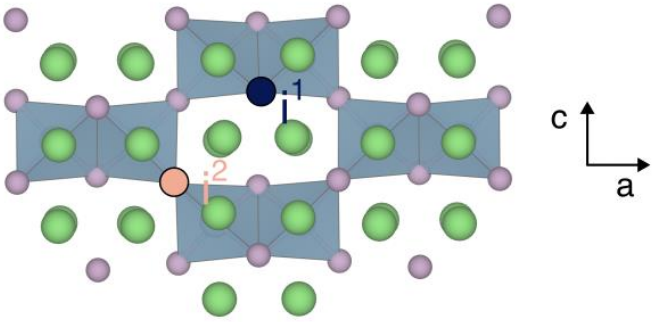

Figure S1.4. Schematic for the two interstitial sites identified from Voronoi decomposition of the crystal structure of Li_3AlP_2 used in defect calculations.

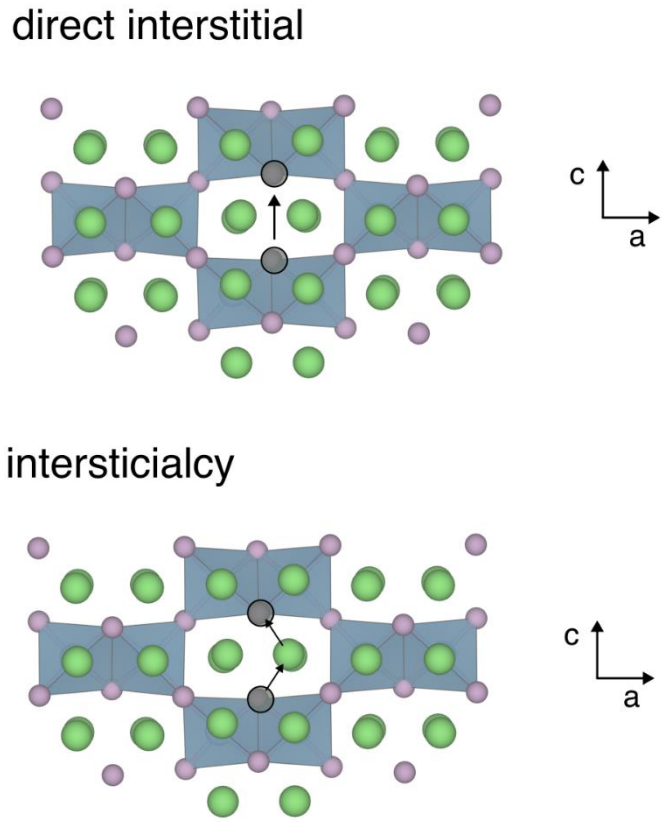

Figure S1.6. schematic showing the interstitial migration mechanisms. The intersticialcy mechanism involves a ”knock-on” process where the migrating interstitial displaces a lithium from its initial site into the second interstitial site.

S1.3 Defect formation energy methodology

Defect formation energies are calculated as

$$\Delta E_f^{X^q} = E_{\text{tot}}^{X^q} - E_{\text{tot}}^{\text{bulk}} - \sum_i (\mu_i + \Delta\mu_i) + q\left(E_{\text{F}} + E_{\text{vbm}} + \Delta V_{\text{pot}}\right) + E_{\text{icc}},$$

where, $E_{tot}^{X^q}$ is the total energy of a supercell containing defect X in charge state q, and E_{tot}^{bulk} is the total energy of the defect free supercell. $\Delta\mu_i$ are chemical potentials of each atomic species i that are added to ($n_i > 0$) or removed from ($n_i < 0$) the supercell to form defect X. μ_i are elemental reference energies, calculated for each element in its standard state. E_F is the Fermi energy, with this term accounting for the energy to add ($q < 0$) or remove ($q > 0$) electrons to or from the supercell. E_{vbm} is the DFT-calculated energy of the valence-band maximum of the host system. ΔV_{pot} is a potential alignment term that accounts for differences in background electrostatic potentials between the host and defective supercells. E_{icc} is the image charge correction term accounting for the Coulombic interactions between defect periodic images. Image-charge corrections were determined using the method of Lany and Zunger and electrostatic potentials were aligned with respect to average core potentials for sets of atoms far from the defect.[1]

To calculate defect formation energies, and hence predict defect concentrations, it is necessary to define the accessible ranges of chemical potentials for the elemental species involved in the formation of each defect.[2] The relevant region of chemical potential space is constrained by the thermodynamic stability limits of the system under study with respect to competing phases and was determined using CPLAP.[3] In the main manuscript, concentrations are presented under the most lithium-poor set of chemical potentials, μ_{Li} = -1.15 eV, μ_{Al} = -1.39 eV, μ_P -0.07 eV. The full chemical potential stability region is shown in Fig S1.7. Defect concentrations are calculated subject to the constraint of net-charge neutrality.[4,5]

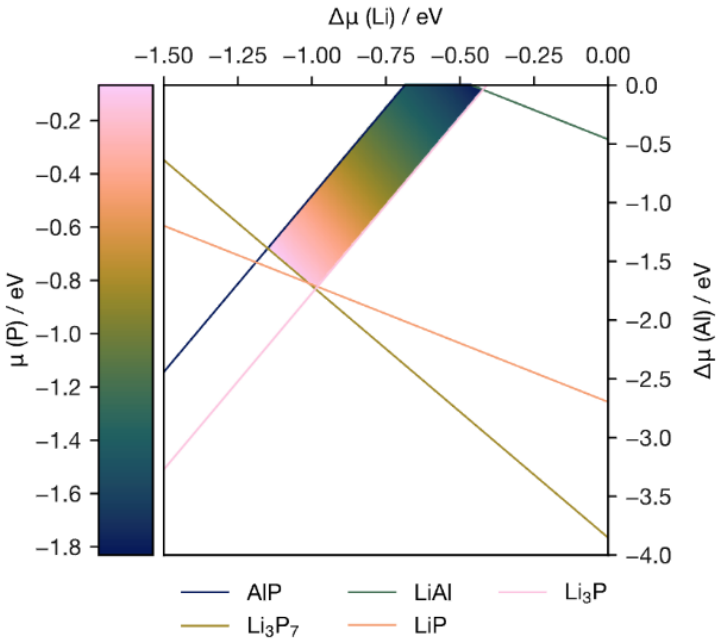

Fig S1.7. The chemical potential stability region of Li_3AlP_2.

S2 Structural refinements

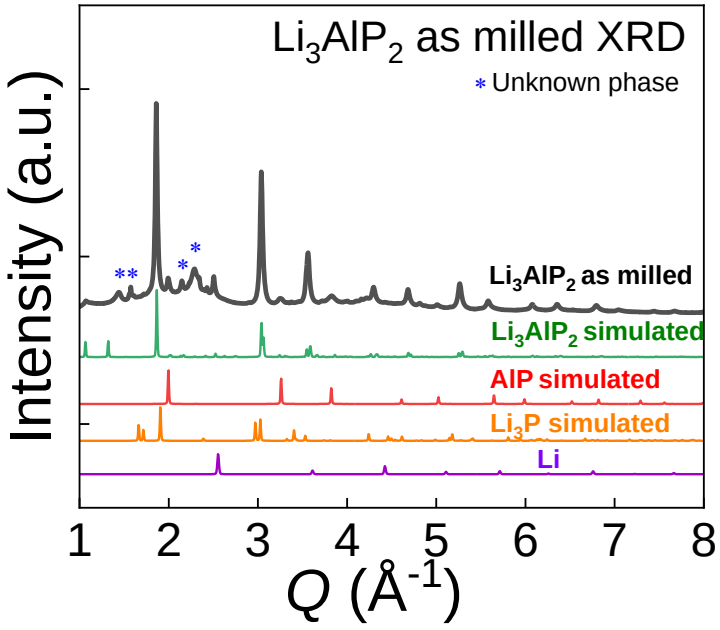

Figure S2.1. Synchrotron XRD for as milled sample at room temperature.

Table S2.1. Structure refinement for μc-Li_3AlP_2 (data shown in main text)

Chemical Formula	Li_3AlP_2
Formula Weight [g mol^{-1}]	109.75
Temperature [K]	300
Wavelength [Å]	λ = 0.17220029
Crystal system	Orthorhombic
Unit cell dimensions [Å]	a = 11.515132 b = 11.759898 c = 5.819406
Volume [Å^3]	788.04
Z	2
Density [g cm^{-3}]	1.85
Q range for data collection [Å^{-1}]	1~5
Refinement method	Rietveld
Goodness of fit	1.07
Profile R indices	R_p= 3.30% R_{wp}= 4.32%
Crystallite size parameter	174.4 nm

Rietveld refinement wars carried out to analysis phase constitution and quantify study of the percentage of the secondary phase. Silicon diffraction pattern was used as calibration to estimate instrumental parameters influence on the peak shape and the peak width for each phase was fitted using Pseudo-Voigt profile. The background of diffraction was fitted through six-degree Chebyshev polynominal. Variables for the fitting were lattice parameters, peak width and the scale factors, while constant parameters selected were isotropic thermal factors, atomic positions and occupancies. The crystallographic information, including lattice parameters,

atomic positions and occupancies for Li_3AlP_2 and Li_9AlP_4 were acquired from the studies of Restle et al.[6,7]

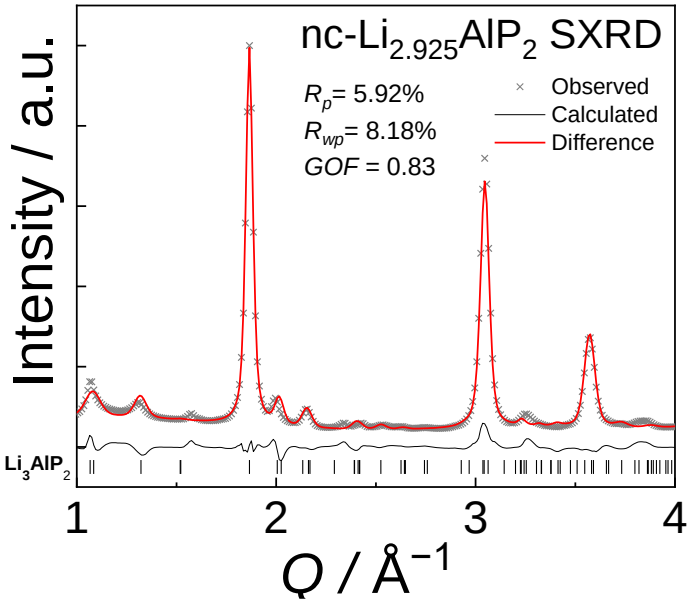

Figure S2.2. Synchrotron XRD refinement for nano-crystalline sample at room temperature.

Table S2.2. Structure refinement for nc-Li_3AlP_2.

Chemical Formula	Li_3AlP_2
Formula Weight [g mol^{-1}]	109.75
Temperature [K]	300
Wavelength [Å]	$\lambda = 0.247968$
Crystal system	Orthorhombic
Unit cell dimensions [Å]	a = 11.69 b = 11.62 c = 5.83
Volume [Å^3]	791.93
Z	2
Density [g cm^{-3}]	1.85
Q range for data collection [Å^{-1}]	1~5
Refinement method	Rietveld
Goodness of fit	0.83
Profile R indices	R_p= 5.92% R_{wp}= 8.18%
Crystallite size parameter	23.17 nm

Rietveld refinement was carried out to quantify the crystallize size for both nc-Li_2AlP_2 and μc-Li_3AlP_2. The crystallite size parameter was determined using the Scherrer equation.[8] The refined crystal domain sizes were 23.17 and 174.4 nm for nc-Li_2AlP_2 and μc-Li_3AlP_2 respectively. It is noted that the Scherrer equation is limited to grain sizes less than 100-200 nm.[8] Therefore the crystallize size for μc-Li_3AlP_2 is consistent with larger, microns-size grains as would be expected.

S2.1 Local structure refinements

Table S2.2. Local structure refinement for nc- and μc-Li_3AlP_2 (data shown in main text)

Chemical Formula	nc-$Li_{3(1+x)}AlP_2$	μm-$Li_{3(1+x)}AlP_2$
R_w [%]	12.96	13.06
Temperature [K]	300	500
Wavelength [Å]	$\lambda = 0.2479$	$\lambda = 0.1239$
Crystal system	Orthorhombic	Orthorhombic
Unit cell dimensions [Å]	a = 11.614552 b = 11.727377 c = 5.822171	a = 11.513879 b = 11.783753 c = 5.821980
Al U_{iso} [Å^2]	0.015344	0.011302
P1 U_{iso} [Å^2]	0.008842	0.007173
P2 U_{iso} [Å^2]	0.008670	0.006333
Scale Factor	0.320083	0.080401
δ1 [Å]	0.881	1.159
Fit range [Å]	2 – 30	2 – 30
SpDiameter [Å]	166.58	146.42

Pair-distribution-function (PDF) analysis was used to determine the local structure of nc- and μc-$Li_{3(1+x)}AlP_2$ from room temperature synchrotron total scattering data. Symmetry and atomic coordinates (x, y, z) from the average structure of the known orthorhombic Li_3AlP_2 phase were fixed, and unit cell parameters and isotropic (U_{iso}) atomic displacement parameters (ADPs) for aluminium and phosphorus sites (P1 and P2) were refined using PDFgui software.[6,7,9] δ1 (Å) is a parameter that describes correlated atomic motions[10] and SpDiameter (Å) is a parameter that accounts for the domains of coherent scattering assuming the domain structure to be spherical. This approach yielded good fits for both phases with weighted residuals of ~ 13% for both the nc- and μc-$Li_{3(1+x)}AlP_2$ materials. All data were fit between 2-30 Å.

S3 MAS NMR spectra

^{6}Li, ^{27}Al, ^{31}P MAS NMR spectra for ball milled Li_3AlP_2 (Fig. S3.1a), nc-Li_3AlP_2 (Fig. S3.1b), nc-$Li_{3.075}AlP_2$ (Fig. S3.1c), d) μc-Li_3AlP_2 (Fig. S3.1d) and μc-$Li_{3.075}AlP_2$ (Fig. S3.1e). All spectra were acquired using the experimental parameters given in the experimental section of the main text. In Figure S3, orange vertical lines indicate resonances corresponding to the crystalline Li_3AlP_2 phase, while green vertical lines indicate impurities. Spinning sidebands in all MAS NMR spectra are marked with asterisks. It can be observed that content of impurities varies across the samples but show no clear trend. The impurities visible in ^{6}Li and ^{27}Al MAS NMR spectra appear at the same chemical shift for all samples, suggesting that these may stem from the same phases appearing in all samples. In case of the impurities visible in the ^{31}P MAS NMR spectra, the ^{31}P resonances at -195 ppm and -240 ppm can only be observed for the μc-Li_3AlP_2 (Fig. S3.1d) and μc-$Li_{3.075}AlP_2$ (Fig. S3.1e) samples, respectively. The origin of the minor phases is unclear.

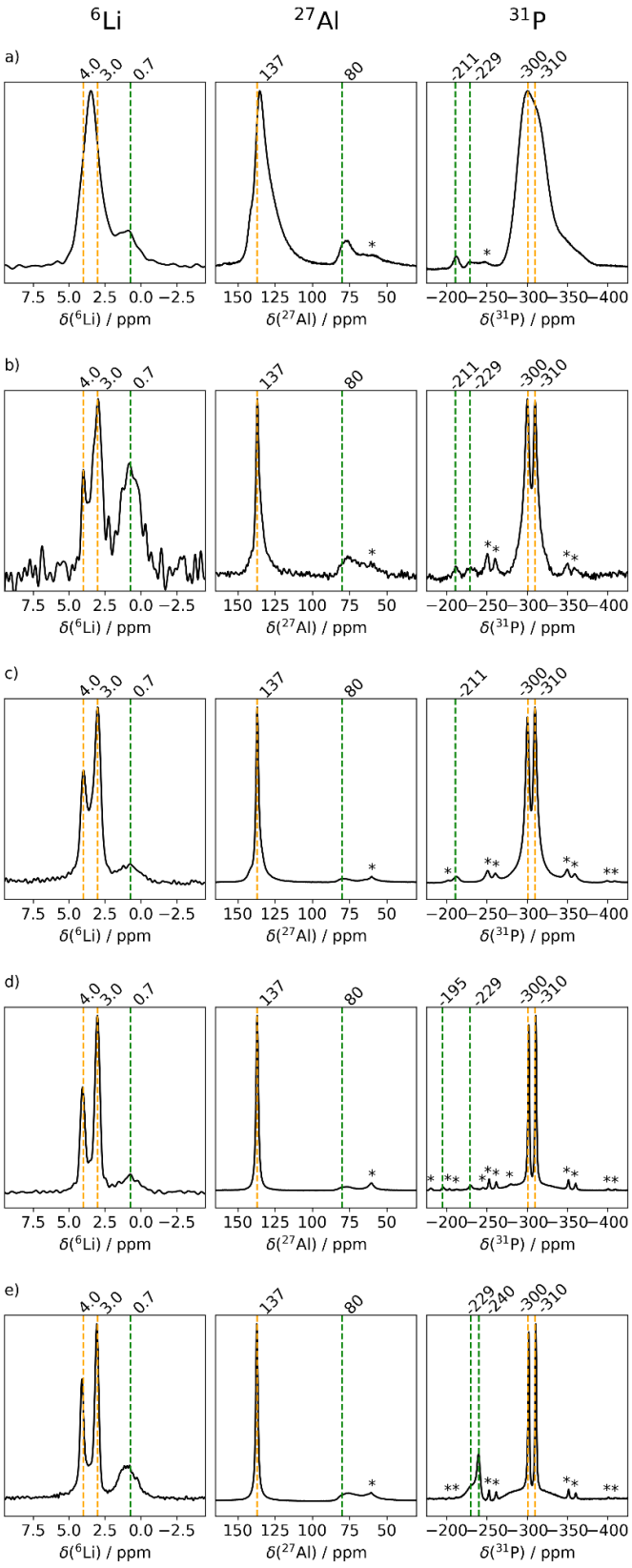

Figure S3.1. ^{6}Li, ^{27}Al, ^{31}P MAS NMR spectra of a) ball milled Li_3AlP_2, b) nc-Li_3AlP_2, c) nc-$Li_{3.075}AlP_2$, d) µc-Li_3AlP_2, and e) µc-$Li_{3.075}AlP_2$ all recorded with a MAS frequency of 10.0 kHz (11.75 T).

S4 NMR dynamics

Normalized ^{7}Li NMR spectra centered at 0 Hz are presented for as milled Li_3AlP_2 (Fig. S4.1a), nc-Li_3AlP_2 (Fig. S4.1b), nc-$Li_{3.075}AlP_2$ (Fig. S4.1c), µc-Li_3AlP_2 (Fig. S4.1d) and µc-$Li_{3.075}AlP_2$ (Fig. S4.1e). The experimental procedure is identical to that used for the samples presented in the main text (Fig. 7) and described in the experimental section. FWHM for the as milled sample is presented in Fig S4.2 and the data were fitted using Equation 1 given in the main text (fit shown with dashed lines in the plot). It can be noted that despite the difference evidence of multiple secondary phases and the sample being amorphous the activation energy for Li^+ transported probed by this experiment remains comparable between all samples. Activation energies of all measured samples are summarized in Table S4.1.

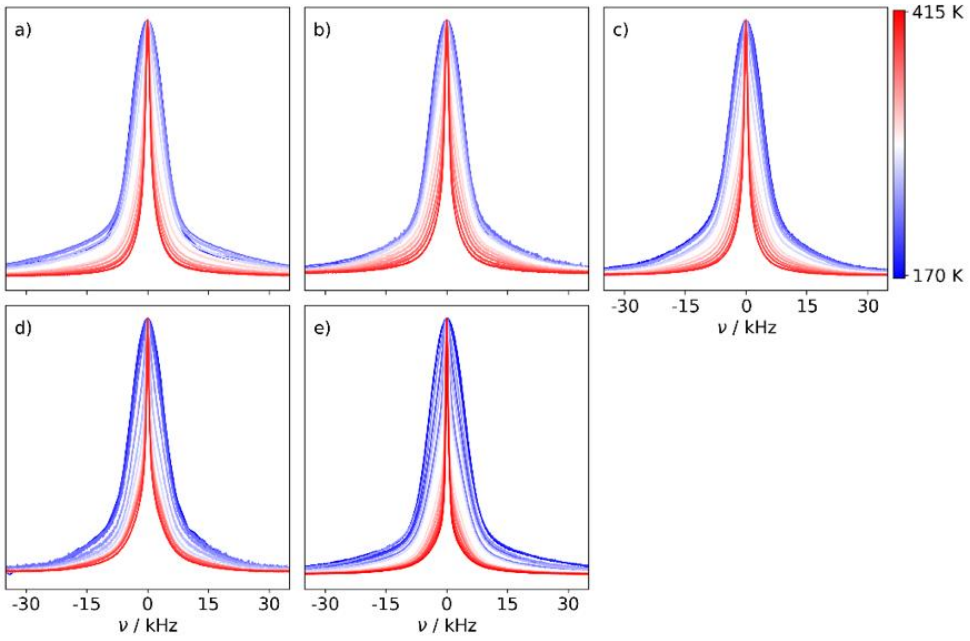

Figure S4.1. Normalized static ^{7}Li NMR spectra for a) as milled Li_3AlP_2 b) nc-Li_3AlP_2 , c) nc-$Li_{3.075}AlP_2$, d) µc-Li_3AlP_2 e) µc-$Li_{3.075}AlP_2$.

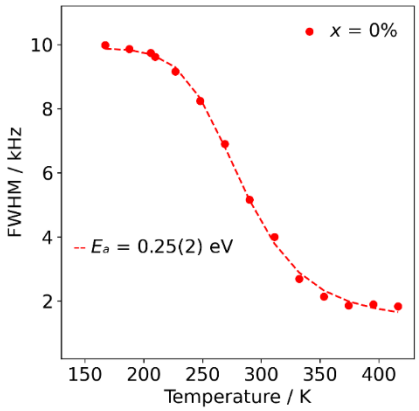

Figure S4.2. FWHM of the static ^{7}Li NMR spectra for ball milled Li_3AlP_2. Data were fit with the Hendrickson-Bray equation (equation 1 in the main text).

Table S4.1. Li hopping activation energy from NMR ion dynamics measurements.

	E_a (eV)		
	$Li_{3.075}AlP_2$	Li_3AlP_2	$Li_{2.925}AlP_2$
As milled	-	0.25 ± 0.02 eV	-
Nano-crystalline	0.25 ± 0.03 eV	0.27 ± 0.03 eV	0.24 ± 0.04 eV
Micro-crystalline	0.24 ± 0.02 eV	0.25 ± 0.02 eV	0.23 ± 0.02 eV

S5 EIS & DRT analysis

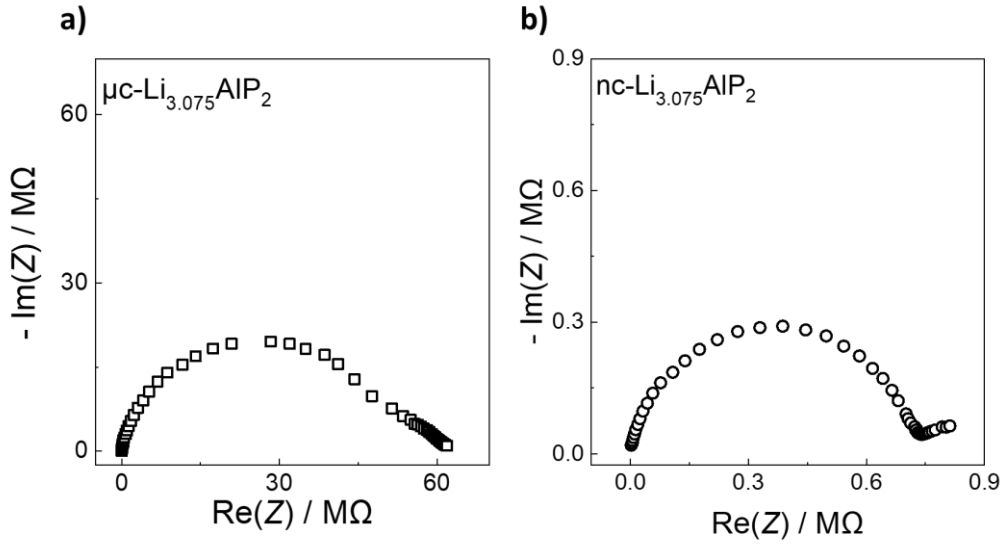

Figure S5.1. Nyquist plots for **a)** μc-$Li_{3.075}AlP_2$ and **b)** nc-$Li_{3.075}AlP_2$ in a Li|SE|Li configuration.

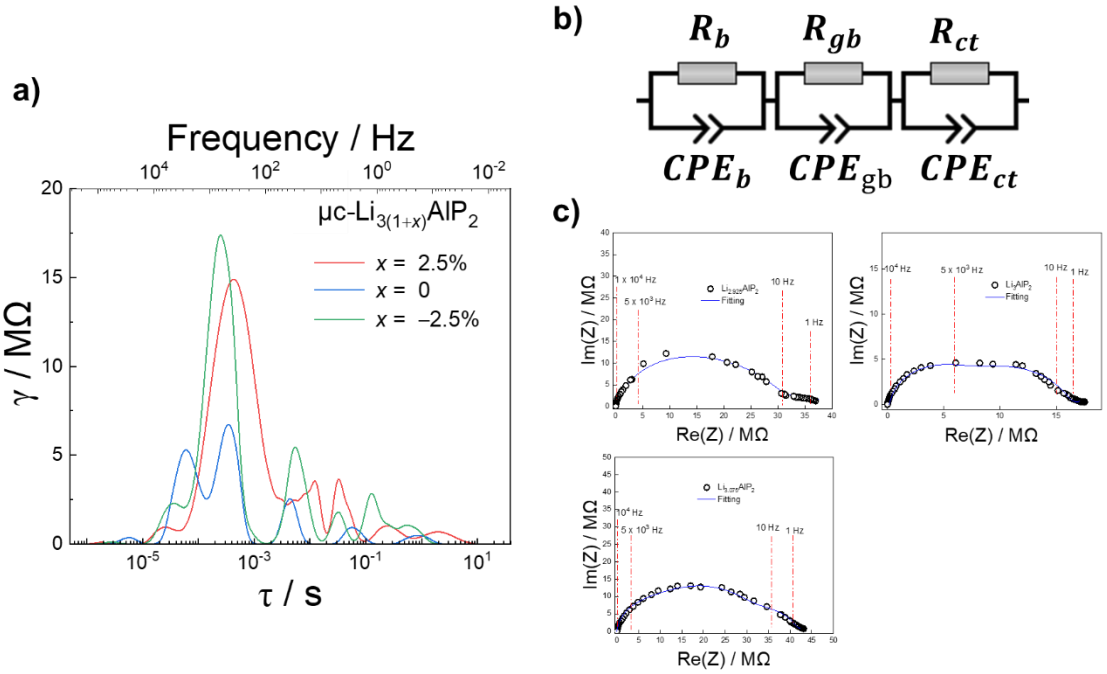

Figure S5.2. a) DRT spectra, **b)** equivalent circuit model used and, **c)** EIS fitting for μc-$Li_{3(1+x)}AlP_2$ samples.

Table S5.1. EIS fitting results for μc-$Li_{3(1+x)}AlP_2$ samples

	R_b /Ω	CPE_b / S· $sec^{\alpha 2}$	α_2	R_{gb} /Ω	CPE_{gb} / S· $sec^{\alpha 3}$	α_3	R_{ct} /Ω	CPE_{ct} / S· $sec^{\alpha 4}$	α_4
$Li_{2.925}AlP_2$	4.2×10^{6}	9×10^{-11}	0.98	2.7×10^{7}	1.0×10^{-10}	0.78	4.6×10^{6}	4.6×10^{-8}	0.79
Li_3AlP_2	6.2×10^{6}	1×10^{-11}	0.98	9.2×10^{6}	1.8×10^{-10}	0.82	1.8×10^{6}	1.8×10^{-8}	0.78
$Li_{3.075}AlP_2$	3.2×10^{6}	8×10^{-11}	0.96	3.2×10^{7}	1.0×10^{-10}	0.82	7.4×10^{6}	2.8×10^{-8}	0.61

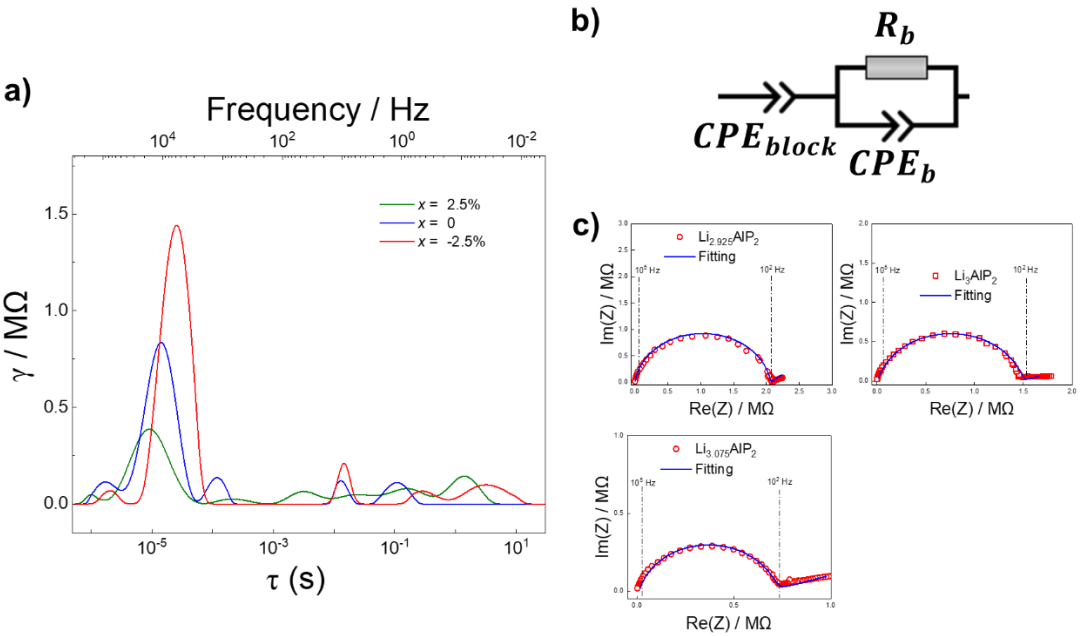

Figure S5.3. a) DRT spectra, **b)** equivalent circuit model used and, **c)** EIS fitting for nc-$Li_{3(1+x)}AlP_2$ samples.

Table S5.2. EIS fitting results for nc-$Li_{3(1+x)}AlP_2$ samples.

	$CPE_{block} / S \cdot sec^{\alpha 1}$	α_1	R_b / Ω	$CPE_b / S \cdot sec^{\alpha 2}$	α_2
$Li_{2.925}AlP_2$	5.375×10^{-6}	0.43	2.06×10^{6}	2.4×10^{-11}	0.93
Li_3AlP_2	5.375×10^{-6}	0.20	1.47×10^{6}	2.88×10^{-11}	0.87
$Li_{3.075}AlP_2$	3.5×10^{-6}	0.20	6.80×10^{5}	4.20×10^{-11}	0.89

S6 Electronic conductivity measurements

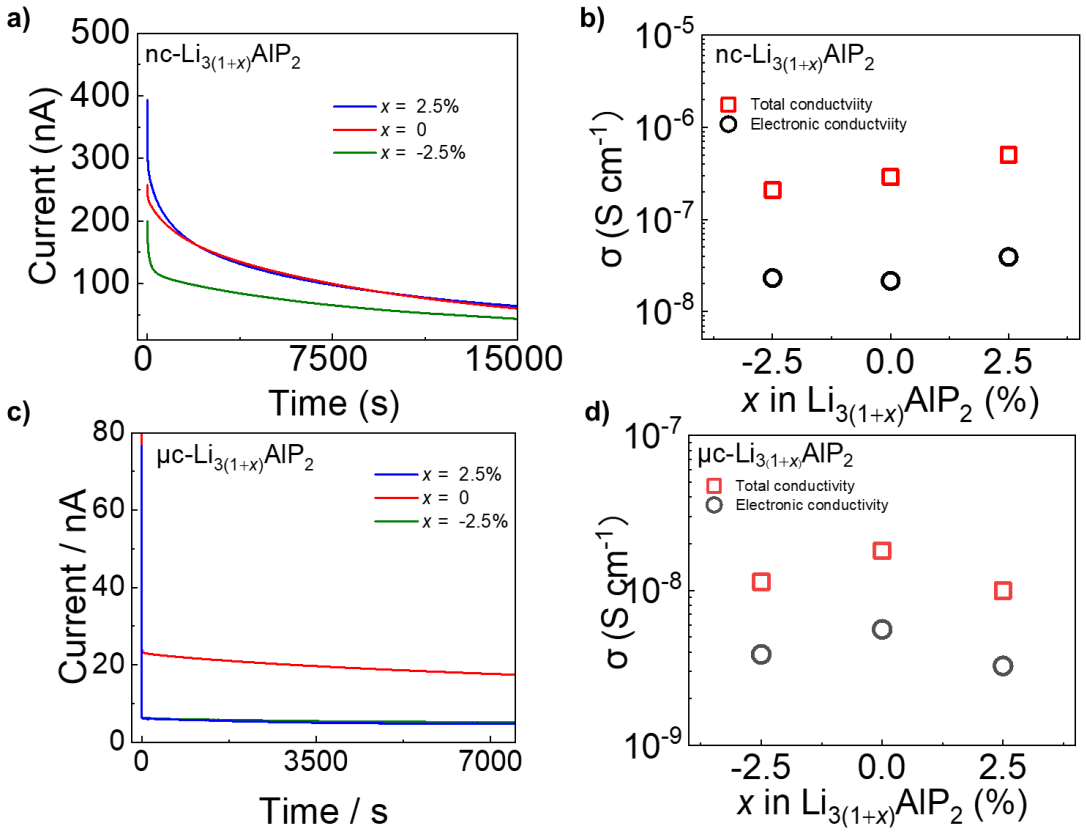

Figure S6.1. DC polarisation and electronic conductivity experiments for **a,b)** nc-$Li_{3(1+x)}AlP_2$ and **c,d)** μc-$Li_{3(1+x)}AlP_2$ samples.

References

[1] S. Lany, A. Zunger, *Phys. Rev. B* **2008**, *78*, 235104.

[2] S. B. Zhang, J. E. Northrup, *Phys. Rev. Lett.* **1991**, *67*, 2339–2342.

[3] J. Buckeridge, D. O. Scanlon, A. Walsh, C. R. A. Catlow, *Comput. Phys. Commun* **2014**, *185*, 330–338.

[4] J. Buckeridge, *Comput. Phys. Commun.* **2019**, *244*, 329–342.

[5] A. G. Squires, D. O. Scanlon, B. J. Morgan, *J. Open Source Softw.* **2023**, *8*, 4962.

[6] T. M. F. Restle, J. V Dums, G. Raudaschl-Sieber, T. F. Fässler, *Chem. Eur. J* **2020**, *26*, 6812–6819.

[7] T. M. F. Restle, C. Sedlmeier, H. Kirchhain, W. Klein, G. Raudaschl-Sieber, V. L. Deringer, L. van Wüllen, H. A. Gasteiger, T. F. Fässler, *Angew. Chemie - Int. Ed.* **2020**, *59*, 5665–5674.

[8] P. Scherrer, *Nachrichten von der Gesellschaft der Wissenschaften zu Göttingen, Math. Klasse* **1918**, *2*, 98–100.

[9] C. L. Farrow, P. Juhas, J. W. Liu, D. Bryndin, E. S. Božin, J. Bloch, T. Proffen, S. J. L. Billinge, *J. physics. Condens. matter* **2007**, *19*, 335219-335219 (7).

[10] I.-K. Jeong, T. Proffen, F. Mohiuddin-Jacobs, S. J. L. Billinge, *J. Phys. Chem. A, Mol. Spectrosc. Kinet. Environ. Gen. theory* **1999**, *103*, 921–924.